Building a Better Anechoic Chamber A Geometric Optics-Based Systematic Solution, Simulated and Verified

Qian Xu, Yi Huang, *Senior Member, IEEE*, Xu Zhu, *Senior Member, IEEE*, Lei Xing, Paul Duxbury, *Member, IEEE*, and John Noonan

***Abstract*—A system-level solution based on geometric optics (GO) for anechoic chamber optimized design is proposed and developed. It can deal with any chamber shape with an arbitrary layout of the radio/radar absorbing material. Two algorithms (forward and inverse) are developed with different complexities for different applications. Two new acceleration strategies in numerical simulation are proposed and implemented. Two semi-anechoic chambers are employed to validate the proposed solution and a good agreement has been achieved between the simulation and measurement results. Furthermore, the limitations of the proposed approach are also discussed. It is proved that the proposed solution is efficient and accurate for anechoic chamber system-level design. The software developed from this work (FACET) could be an effective and efficient solution for the industry.**

***Index Terms*—Anechoic chamber design, geometric optics (GO), normalized site attenuation (NSA).**

I. Introduction

An anechoic chamber is a large room lined with radio/radar absorbing materials (RAMs) on the boundaries to simulate the free space environment – no radiowave echoes are generated, it has been widely used in the electromagnetic (EM) community for many years in applications from mobile phones, antennas, EMC tests to stealth aircraft and radar measurements [1]. However, the design of anechoic chambers is difficult and heavily dependent on the designer's experience [2]. Normally, a large safe margin is built in to ensure the good performance of the chamber. There is a trade-off between the performance and the cost, the better RAM (thus better chamber performance) normally means more expensive and a larger RAM size. At the moment, there are no proper chamber design tools available; all chambers are basically designed using some guidelines (including in-house simple tools) and experience. The objective of this work is to develop an efficient and systematic solution for anechoic chamber design which will help the designer to estimate the chamber performance accurately during the design process. The ultimate goal is to minimize the cost but optimize the chamber performance for given conditions and specifications.

The chamber may have various forms in applications, such as tapered chambers [3], compact chambers with reflectors [4], double horn chambers [5], [6], *etc*. There are many ways and parameters to characterize the chamber performance: site attenuation (SA, or normalized SA), site voltage standing wave ratio (SVSWR) and field uniformity (FU) are the three key parameters which are normally employed in the chamber related standards [7], [8] to evaluate the chamber performance.

A number of computational electromagnetics (CEM) modeling methods have been employed for chamber simulation, and they can be divided into two classes: micro level and macro level.

At the micro level, the RAM reflectivity is related to the shape, permittivity and permeability of the RAM, full wave methods such as the finite-difference time-domain (FDTD) [9], frequency-domain finite-difference (FDFD) [10], finite element method (FEM) [11], and integral equation (IE) [12, 13] have been applied to the simulation and optimization of the RAM. By taking advantage of the periodic boundary condition, the mesh number and memory requirement can be reduced significantly. Other methods used for this problem, like the transmission line method [14], homogenization method [15-17] and rigorous coupled-wave analysis [18], simplify the RAM structure under certain assumptions. These methods may combine the analytical and numerical strategies together to further reduce the memory and time consumption with the expense of accuracy.

At the macro level, the whole chamber performance is considered. Full wave methods have also been applied, because of the complexity and the large electrical size of the whole chamber, simplifications have been made to increase the efficiency and reduce the time and memory requirement. For example, in [19], to avoid the calculation of the Green's function in such a complex environment, conductive wire meshes have been used to imitate the RAM in the moment method (MoM); in [20], large cells were introduced to increase the time step and reduce the memory requirement in the FDTD

Manuscript received April 3, 2015. This work was supported in part by the Centre for Global Eco-Innovation with project No. 139 and MVG (Microwave Vision Group). Corresponding author: Y. Huang.

Q. Xu, Y. Huang, X. Zhu and L. Xing are with the University of Liverpool, Department of Electrical Engineering and Electronics, Liverpool, L69 3GJ, UK (e-mail: qian.xu@liv.ac.uk; yi.huang@liv.ac.uk; xuzhu@liv.ac.uk; l.xing@liv.ac.uk).

Paul Duxbury and John Noonan are with the MVG., Lakeside Court, Haydock Lane, Haydock, WA119 UY, UK (e-mail: paul.duxbury@rainfordemc.com; john.noonan@rainfordemc.com).

method; the homogenization method can also be combined with the transmission line matrix (TLM) to boost the efficiency [21]. Brute-force full-wave models without any simplifications have been applied as well, such as the TLM [22], hybrid MoM/FEM [23] and FDTD [24]. Even with a high performance computer, large electrical size problems with complex material scenarios are not easy to solve due to the large memory and time requirements.

High frequency approximation methods such as GO have been proven to be a fast and efficient way to simulate the macro level problem [25-30]. However, RAM modeling at the system level is normally simplified by using a cosine approximation [26], an effective medium [31], a homogenization model [15], [16] or a multi-layer model [27]. Thus, the RAM is not fully described and to find an accurate equivalent analytical model over a wide frequency range and a wide incident angle is challenging.

In this paper, we deal with the chamber design problem at the macro level and aim to develop an efficient and flexible system-level CAD tool. A full numerical model is used to describe the characteristics of the RAM without losing accuracy and efficiency. The GO theory is introduced first, and two different algorithms (forward and inverse [32]) are then developed with different acceleration strategies in the simulation, the far-field pattern of the antenna is used as the excitation source rather than a 3D antenna model as in the full wave simulation. This is reasonable because normally the antenna manufacturer needs to protect their intellectual property (IP) and does not provide the detailed 3D model of the antenna. The same thing applies to the RAM, the reflection coefficient of the RAM will be used rather than a simplified model or 3D model, it will be fully considered as a function of polarization, frequency, and incident angle; each type of the RAM will be saved as a multidimensional matrix. By borrowing the philosophy of object-oriented programming (OOP), from the system-level point of view, sub level objects like antennas and RAMs are encapsulated and easy to reuse. Finally, the results are verified by both simulations and measurements.

II. Theory

A. Geometric Optics

Compared with other CEM algorithms, GO may have the simplest expression in mathematics as shown in [33], [34]. The E-field in the chamber can be expressed as

$$\vec{E} = \vec{E}_0 \cdot \left\{\prod \bar{\bar{R}}_i\right\} \cdot \left\{\prod \bar{\bar{T}}_i\right\} \cdot \left\{\prod e^{-\gamma_i l_i}\right\} \cdot SF \qquad (1)$$

where the E-field is assumed to propagate like the light as shown in Fig. 1 where A_0 and A are the cross-sectional area of the ray tubes at the source point and field point of interest, they will be used to calculate the spreading factor ($SF = \sqrt{A_0}/\sqrt{A}$). $\vec{E}_0$ is the E-field at the source point (reference point), $\vec{E}$ is the E-field at the field point. $\prod \bar{\bar{R}}_i$ and $\prod \bar{\bar{T}}_i$ are the reflection and transmission coefficient dyads along the whole ray path, $\prod e^{-\gamma_i l_i}$ is the total phase variations and losses along the whole path.

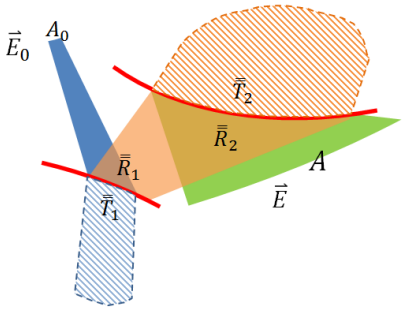

Fig. 1. Radio wave propagation in GO.

It can be seen from Fig. 1 that once the ray path is obtained, it is easy to calculate the E-field at the field point. For the anechoic chamber simulation, no transmission coefficient needs to be considered, this simplifies (1) as

$$\vec{E} = \vec{E}_0 \cdot \left\{\prod \bar{\bar{R}}_i\right\} \cdot \left\{\prod e^{-\gamma_i l_i}\right\} \cdot SF \qquad (2)$$

where $\bar{\bar{R}}$ relates the incident field $\vec{E}^i$ and reflected field $\vec{E}^r$ as

$$\vec{E}^r = \begin{bmatrix} E_\parallel^r \\ E_\perp^r \end{bmatrix} = \bar{\bar{R}} \cdot \vec{E}^i = \begin{bmatrix} R_{\parallel\parallel} & R_{\parallel\perp} \\ R_{\perp\parallel} & R_{\perp\perp} \end{bmatrix} \begin{bmatrix} E_\parallel^i \\ E_\perp^i \end{bmatrix} \qquad (3)$$

where $E_\parallel$ and $E_\perp$ are the decomposed parallel component and perpendicular component of the E-field. Equation (2) also simplifies the data structure for the CAD tool. In the simulation, this procedure requires a stack to store the rays, once the first ray of the stack is popped and traced, two rays are pushed back to the stack, this process will continue until the stack depth becomes zero. Without considering the transmission rays, the total ray number is not changed during the simulation; the rays can be stored in arrays.

B. Ray Tracing

The ray tracing technique has been well developed in the computer graphics community [35]. Although many techniques can be applied to EM simulation, no codes can be used directly without modification, and the biggest difference may be the polarization and field superposition.

Normally, ray tracing technique can be divided into two groups: forward and inverse algorithms [32] as shown in Fig. 2.

For the forward algorithm, the E-field on a predefined monitor plane is recorded, it can deal with point-to-area (P2A) problems but the inverse algorithm is more efficient for point-to-point (P2P) problems, only the E-field of the predefined points is recorded [36]. The bottleneck for the forward algorithm is the speed in finding the intersection point between the ray and model. For a single ray, the complexity is $O(NM)$ (N is the number of patches describing the model, M is the reflection order) without using an acceleration technique. It can be reduced to $O(NM/2^H)$ (H is the depth of octree) by

using octree [37], or $O(Mlog_2N)$ by using kd-tree technique [38], and it can be further reduced by taking the advantage of ray coherence theorem [36], [39]. Other techniques include parallelization with graphics processing unit (GPU) [40] and multi-resolution grid to reduce the total ray number [41]. The bottleneck for the inverse algorithm is finding the path that connects the source and field points with different orders, the maximum complexity is $O(N^M)$ [42].

It is important to note that the complexity discussed above is for a single ray. If we consider the ray number T related with the electrical area S of the chamber as $T \sim O(S^2) \sim O(f^2)$ (f is the frequency of interest), and the frequency sweep with F points the complexity of the forward algorithm needs to be multiplied by a factor of $O(Ff^2)$. However, for the inverse algorithm, the ray path between the source point and the field point can be recorded after path finding, this makes it nearly independent of F and f, and the complexity will not be affected too much.

In this paper, both algorithms are developed with the acceleration techniques; the chamber designer can choose the suitable one for a specific problem. If the field distribution in a specific region is of interest, the forward algorithm is preferred, if only the field at some discrete points need to be known, the inverse algorithm is more efficient. Different from other full-wave methods, the beauty of GO is that the fields contributed by different orders can be separated. The designer can identify where the unexpected field comes from by analyzing the field with different orders.

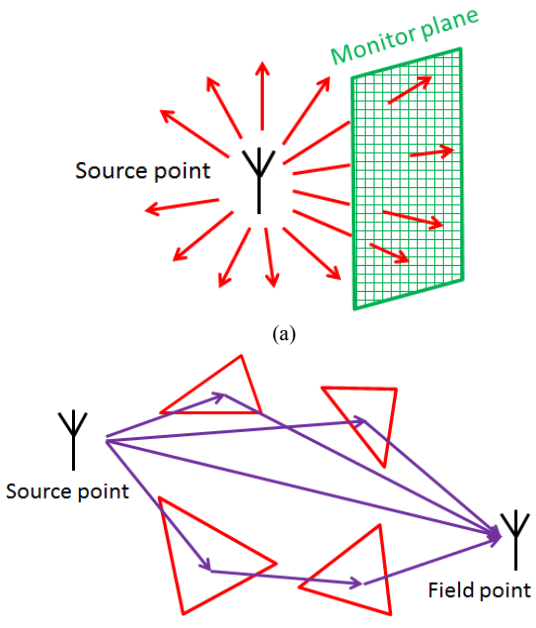

Fig. 2. Two different approaches in ray tracing: (a) forward algorithm, (b) inverse algorithm.

III. Simulation

The proposed solution diagram is given in Fig. 3, which includes four parts from the top to the bottom. We name the software based on this solution as the *fast anechoic chamber evaluation tool* (FACET). The graphical user interface (GUI) is developed by using Microsoft Visual Basic .NET and the computational engine is developed by using MATLAB. They are connected using component object model technology. Like other CEM tools, it includes preprocessing, simulation and post processing parts. The two different algorithms share the same preprocessing but different post processing part. Each part will be explained in details.

A. Modeling

The model of a chamber is described by an ASCII STL file [43]. After importing the STL file, the model will be discretized into triangular meshes on the surfaces as shown in Fig. 4. The meshes will be used to determine the intersection point between the ray and the model.

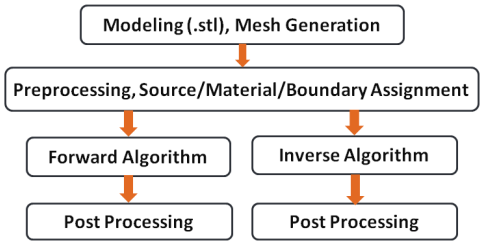

Fig. 3. Block diagram of the proposed solution.

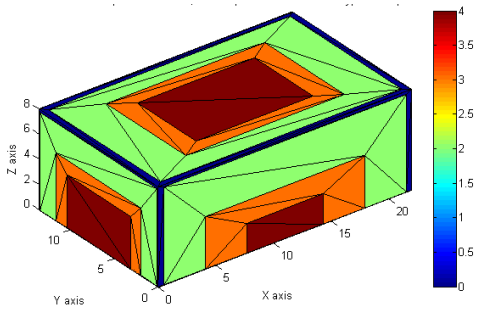

Fig. 4. Discretized chamber model with different RAMs (represented by the colors in different regions).

B. Preprocessing

1) Building the Octree: An octree is a data structure and suitable for the forward algorithm. We follow the same process given in [37]. But different from [37], we propose an adaptive octree depth instead of a fixed depth octree. The depth (D) is given as

$$D = 1 + \left[log_2 \frac{max(W, H, L)}{mean(Triangle\ edge\ length)} \right] \quad (4)$$

where W, H and L represent the width, height and length of the chamber respectively, the mean value of all triangle edge length is used to determine the depth of the octree. The complexity of the octree building process is $O(ND)$, no acceleration technique is necessary, and the octree only needs to be built once.

2) Far-field Data: The antenna far-field pattern is considered as the excitation source of the chamber; the E-field at 3 m distance is calculated as $\vec{E}_0$ in (2). As we can see, the structure

of the antenna is encapsulated; only the far-field data is needed, which can be obtained from either simulation or measurement of the antenna. To make it reusable, once the far-field pattern is obtained, it will be saved into a library/database which can be reused for future simulations. Four matrices are used to save the complex electric far-field at each frequency. They are $[E_{\theta mag}]$, $[E_{\theta phase}]$, $[E_{\varphi mag}]$ and $[E_{\varphi phase}]$ with dimension R x C where R is number of points in φ (azimuthal angle) direction, C is the number of points in θ (polar angle) direction.

3) Boundary Condition: If we borrow the philosophy of the OOP, each triangle can be considered as an object in programming and the type of RAM on it can be considered as its property. Different triangles may have different kinds of RAM, as shown in Fig. 4.

The boundary conditions in the full wave simulation normally include the perfect electric conductor (PEC), perfect magnetic conductor (PMC), radiation condition or perfect matched layer (PML), *etc.* In GO we can also emulate these kinds of boundary conditions by assigning suitable values to the reflection coefficient matrix $\bar{\bar{R}}$ which has taken the wave polarization into account as shown in (3). The coordinates are defined in Fig. 5. The $\bar{\bar{R}}$ for the PEC is

$$\bar{\bar{R}} = \begin{bmatrix} R_{\parallel\parallel} & R_{\parallel\perp} \\ R_{\perp\parallel} & R_{\perp\perp} \end{bmatrix} = \begin{bmatrix} 1 & 0 \\ 0 & -1 \end{bmatrix} \tag{5}$$

For the PML, there are two ways to treat it, we can either set the reflection coefficient to a very small value (e.g. -200 dB) or mark it a special type. In this paper, we set the RAM type index as -1, which can make it faster in ray tracing, and all rays that hit on the PML do not need to be traced for the next order reflection.

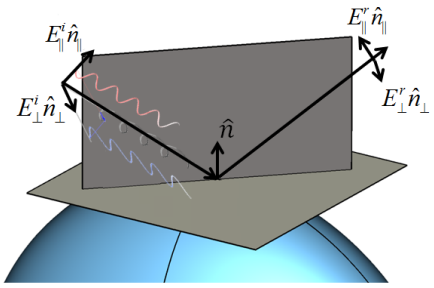

Fig. 5. Definition of the coordinates for the incident and reflected wave.

4) RAM Definition: A full numerical model is proposed to describe the reflection coefficient of the RAM, the reflection coefficient dyad $\bar{\bar{R}}$ includes 4 elements: $R_{\parallel\parallel}$, $R_{\parallel\perp}$, $R_{\perp\parallel}$ and $R_{\perp\perp}$, all of them are dependent on the incident angle and frequency, $R_{ij} = R_{ij}(\theta, \varphi, f)$ (i, j can be $\parallel$ or $\perp$), a 3D matrix as shown in Fig. 6 is used to save each type of RAM.

Compared with the traditional simplified models [14-17], this approach needs more memory (10 MB/each RAM type) but much faster than the simplified models which need more operations to calculate the reflection coefficient for each reflection (while the proposed approach only needs interpolation). Also the proposed numerical model encapsulates the detailed information of RAM which can be obtained from either simulation [9-18] or the arch method in measurements [44]. The information is saved in a library/database to make it reusable.

The RAM layout definition process is the same as the boundary condition definition. The type index is used to mark the RAM type on each triangle. The rotation of RAM is considered by applying an angle offset to R_{ij} with $\Delta\varphi$ ($R_{ij}(\theta, \varphi + \Delta\varphi, f)$).

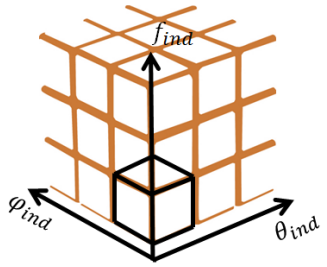

Fig. 6. Data structure of the reflection coefficient.

C. Forward Algorithm

In this section, the forward algorithm is detailed with the acceleration techniques. First, the rays are launched from the source point, and then reflected and intercepted by the monitor plane as shown in Fig. 2; finally, results from different reflection orders are superimposed to obtain the total E-field.

1) Initial Value: The initial value of the E-field and cross-sectional area need to be known to start the ray tracing procedure. The sphere surrounding the source point is divided into triangular patches as shown in Fig. 7. The vertices of the patch and the center of sphere form a tetrahedral, as shown in Fig. 8. The initial value $\vec{E}_0$ is determined by the E-field on the sphere using 2D interpolation of $[E_{\theta mag}]$, $[E_{\theta phase}]$, $[E_{\varphi mag}]$ and $[E_{\varphi phase}]$, the radius of the sphere can be an arbitrary value, we use 3 m. The initial cross-sectional area is the triangular area A_0 which will be used to calculate *SF* later; different from the pyramid ray tube in [34], the tetrahedral ray tube is used. For a pyramid ray tube, the wave front is quadrilateral, there is a potential risk that the wave front will be distorted and self-intersected after reflecting by the model, but for the tetrahedral ray tube, the wave front is always kept the shape of triangle. After the ray and ray tube is traced, $\vec{E}$ at the field point is determined using (2).

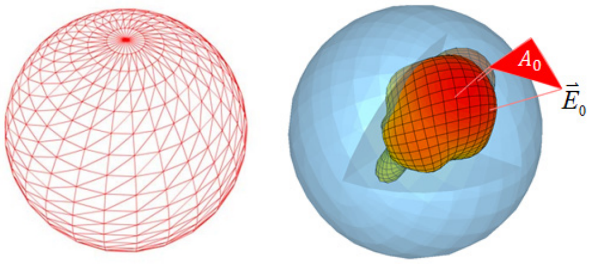

(a) (b)

Fig. 7. (a) Sphere division and (b) initial values.

It is interesting to note that each tube shares the same vertex with its neighbor, but the *SF* can be different after the tube interacts with the model, this will make the E-field at the vertices ambiguous. To eliminate this ambiguity, we only use the vertices to carry the information of *SF*, the E-field is defined at the sample points inside each patch, as shown in Table I, the tube triangle is divided into different orders, and the sample points are chosen to be the center of each triangle.

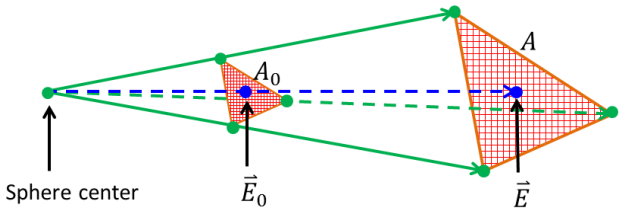

Fig. 8. E-field along the ray.

TABLE I
TRIANGLE WITH DIFFERENT DIVISION ORDER

Division Order	Number of Sample Points	Triangle Division
1	1	
2	4	
3	16	
⋮	⋮	⋮
n	4^{n-1}	

2) Ray Tracing: After the initial value of the E-field is determined, rays need to be traced and recorded at the monitor plane. Since the adaptive octree has been built in the preprocessing part, we use the famous breadth-first search (BFS) algorithm [46] to find the intersection point between the ray and the model. Fig. 9 gives the searching process of BFS algorithm.

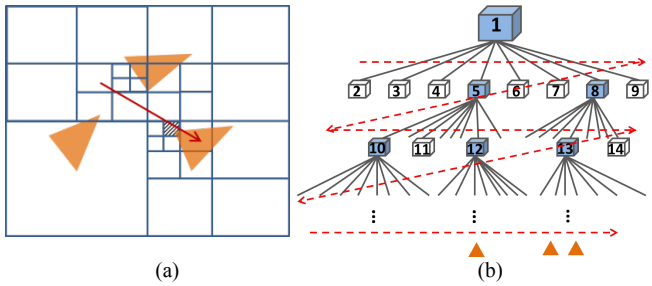

(a) (b)

Fig. 9. BFS searching algorithm: (a) geometrical view, (b) hierarchical view.

The model is divided into boxes with hierarchy, the ray can be launched from anywhere in the model. The boxes at the top level are first checked. If the ray intersects with it, check the sub level boxes. In the last level, the intersection between the ray and triangle is checked (the shaded area in Fig. 9(a)), because the ray-box intersection check is much faster than the ray-triangle check. Fig. 9(b) gives the searching direction and sequence number, the shaded area means the box containing triangles that may potentially intersect with the ray.

It is important to note that: if the model is over-divided by octree (the octree level is too deep), the searching speed will deteriorate. The ray-triangle and the ray-box checking numbers with different octree depths are given in Fig. 10. The model contains 768 triangle meshes, 1000 random rays are launched to perform the benchmark. When the octree depth is 1, the model is not divided into an octree; the ray-box checking number is zero. As can be seen in Fig. 10, although deeper octree reduces the ray-triangle checking number, it increases the ray-box checking number thus more time is wasted on the ray-box intersection check. That is the reason why the adaptive octree is proposed.

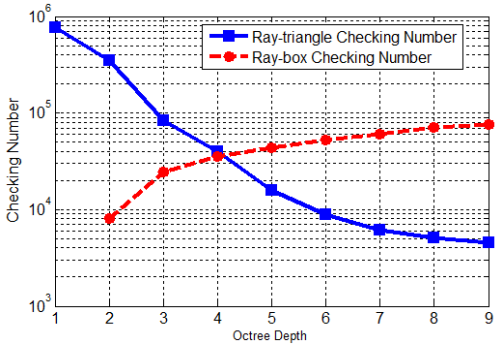

Fig. 10. Ray-triangle and ray-box checking numbers with different octree depth.

3) Reflection Coefficient Interpolation: Once the intersection point between the ray and the triangle is found, equation (3) is used to calculate the reflected E-field and update the initial value and the wave front area A_0 for the next trace. Because the incident angle can be of an arbitrary value and the frequency of interest may not be exactly the same as the sample frequency in the full numerical model of RAM (where a set of frequencies are used), 1D and 2D interpolation are used to obtain the reflection coefficient value. First, each matrix in $\bar{\bar{R}}$ is interpolated with the frequency of interest, since each element in the matrix needs to be interpolated, it is time consuming to do it in the ray tracing loop. This procedure can be moved out of the ray tracing loop and it only needs to be calculated once for each frequency of interest. Then, the 2D angle interpolation is applied to each matrix in $\bar{\bar{R}}$. Considering the magnitude and phase, this makes only eight 2D interpolations for each ray-triangle intersection, which is much faster than the traditional RAM model.

4) Acceleration Techniques: One of the advantages of GO is that it is easy to parallelize. We have already used the octree algorithm to accelerate the intersection checking process. Further acceleration techniques are also considered, both the distributed computing and multithreading techniques are employed to divide the sphere in Fig. 7(a) into sub regions; rays in different sub regions are traced simultaneously in a different

computing engine, and finally the results are combined. Two methods are used to reduce the number of the total rays: one method is to set a threshold for the E-field value (e.g. -30 dB of the peak value). The rays below the threshold will be skipped. Another method is to limit the ray launching region; we rarely need to consider the rays close to the polar points in Fig. 7(a). By combing these two methods the speed can be improved significantly.

5) Superposition: After the monitor plane is defined, the plane needs to be discretized into meshes. The mesh size is normally chosen $\leq \lambda/10$ (λ is the wavelength of the frequency of interest). Fig. 11(a) gives the procedure for the value assignment in each tube: the values on each grid are first initialized as zero, after the ray tube is intercepted by the monitor plane, the grid points in the tubes are checked, the distance between the grid points and the sample points are calculated, the E-field of the nearest sample point is chosen to be the value of the grid point. Fig. 11(b) shows the superposition of the field values between two tubes, the field value on the grid points shared by different tubes are superimposed.

Finally, the E-field from different orders needs to be superimposed to obtain the total value.

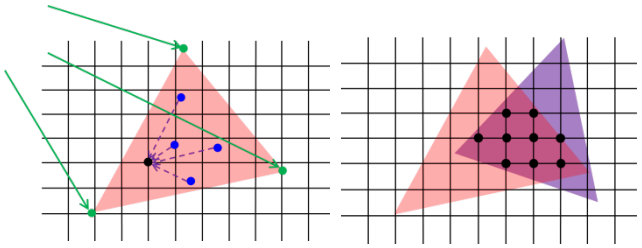

(a) (b)

Fig. 11. Superposition of the E-field in different tubes: (a) value assignment in each tube, (b) value update for the grid points shared by different tubes.

D. Inverse Algorithm

Different from launching the rays in all directions in the forward algorithm, the inverse algorithm finds the path that connects the source point and the field point which is called path finding. After the paths are found and saved, the initial value and the reflection coefficient can be obtained in the same way as in the forward algorithm, the final E-field with different orders can also be easily superimposed.

1) Path Finding: Each triangle has a unique index number; the possible paths to be checked are shown in Fig. 12. For the rays reflected once from source point (*S*) to field point (*F*), the possible paths are *S*-1-*F*, *S*-2-*F*, *S*-3-*F* and *S*-4-*F*. As can be seen in Fig. 12(a), only 2 paths are practical (visible), other images are invisible because the intersection points are outside the triangle. The same thing happens to the 2nd order rays in Fig. 12(b), the number of paths to be checked becomes 12. Generally, for the model with *N* triangles, the number of *Mth* order paths to be checked is $N(N-1)^{M-1}$ [32], [42]. It is important to note that without any acceleration strategy, it could be very time consuming to check the images one by one when *N* and *M* are large numbers.

2) Acceleration Techniques: Parallelization is used as shown in Fig. 13. The engine can be a distributed computer or a thread in a single computer. The whole path tree is split into different parts which are checked by different engines simultaneously.

An additional strategy which takes advantage of the chamber shape is proposed and called convex acceleration. In topology, the 3D model can be divided into two categories: the concave and the convex as shown in Fig. 14.

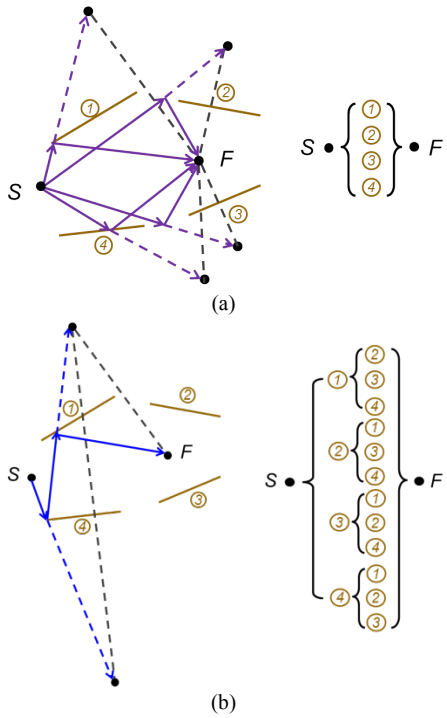

Fig. 12. Path finding in the inverse algorithm: (a) paths with the 1st order, (b) paths with the 2nd order.

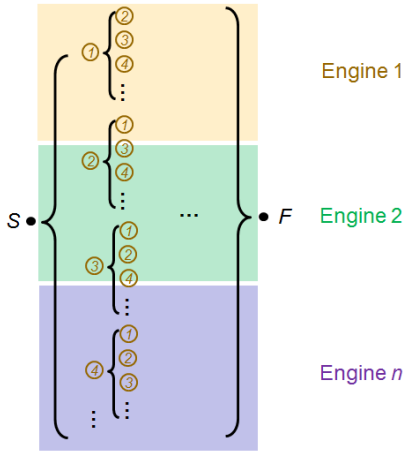

Fig. 13. Parallel path finding.

For a convex shape, all line segments connecting any pair of points are inside the shape. For a concave shape, there is a possibility that the line segments will be intercepted by the model itself. This offers an opportunity to accelerate the path finding process. Generally speaking, each path needs to be checked to make sure it is not intercepted by the other triangles of the model, but for a convex model, this checking procedure

is not necessary since most of the chambers are convex shape. The benchmark has been performed to validate the convex acceleration: for a model with 116 triangles, 1 thread is used, and only the 1st order reflection is considered, we found that the speed with convex acceleration is 28 times faster than the general algorithm.

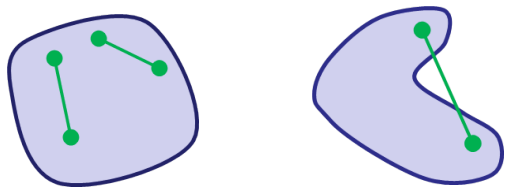

(a) (b)

Fig. 14. Topology of the model: (a) convex shape, (b) concave shape.

E. Post processing

The post processing is to process the results and calculate the figures of merit such as the SA in a fully anechoic chamber, or NSA in a semi-anechoic chamber, SVSWR and FU. All of these values are extracted from the E-field distribution in the post processing part. If the transmitting (Tx) antenna is well matched and the input power is normalized to 1 W, the NSA value can be calculated by using [45]

$$NSA(dB) = 46.76 + G - 20logf - 20logE_{max} \quad (6)$$

where G is the gain of the Tx antenna in free space in dBi, f is the frequency of interest in MHz, E_{max} is the maximum E-field value in V/m measured by the receiving (Rx) antenna, when the height is scanning from 1 m to 4 m. The definitions of SVSWR and FU can be found in [7], [8].

For a semi-anechoic chamber, the NSA is required to be in the range of ±4 dB of the values given in the standard [7], the SVSWR is required to be ≤ 6 dB and the FU is required to be in the range of 0 dB to +6 dB for 75% of the sample points for each frequency (shown in Table II).

TABLE II
ACCEPTABILITY CRITERION

Test Performed	Acceptability Criterion	Reference
NSA	±4 dB	[7]
SVSWR	≤6 dB	[7]
FU	-0 dB, +6 dB for 75%	[8]

The cost of RAM used in the chamber can be obtained by

$$Cost_{RAM} = \sum Area_i \times Price_i \quad (7)$$

which is the summation of the price for all the RAMs used in the chamber, where i means the type index of the RAM. The cost is a vital parameter for a business, especially when the chamber is large. The proposed solution can optimize a chamber for given specs.

IV. VERIFICATION

A semi-anechoic chamber as shown in Fig. 15 is used for evaluation. The size of the chamber is 22 m × 13.5 m × 8 m ($L \times W \times H$). The Rx antenna is positioned at the left side in the test region, the Tx antenna is 3 m away from the Rx antenna, the height is 2 m. Both Rx and Tx antennas are half-wave dipoles. All the boundary conditions are set as PML except the ground plane (set as PEC). A monitor plane is set at $x = 15.45\ m$ across the center of the test region to record the E-field.

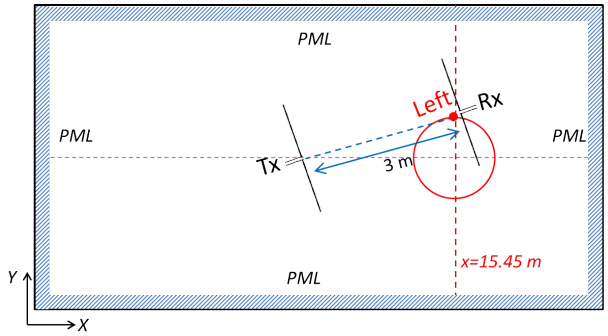

Fig. 15. A cross-section (horizontal) view of an ideal semi-anechoic chamber.

Since this is a perfect half-space problem, and the Green's function for the half space is well-known, only the Tx antenna needs to be discretized and the MoM is used to simulate it. Then, the far-field data is exported to FACET to predict the chamber performance; the results obtained from FACET and MoM method are compared to verify the accuracy of the proposed solution. The magnitude of the total E-field on the monitor plane at 1 GHz is shown in Fig. 16. As can be seen, they are in good agreement.

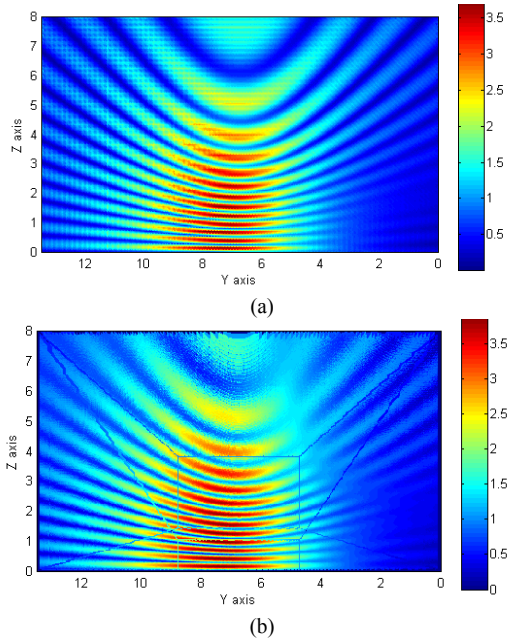

Fig. 16. Total E-field in the semi-anechoic chamber: (a) obtained by using MoM method, (b) obtained by using the forward algorithm.

The small difference between Fig. 16(a) and Fig. 16(b) is

due to the mutual coupling of the mirror antenna. The mutual coupling between the Tx antenna and its mirror antenna was considered in MoM, but not in FACET. A unique feature of GO is that the fields with different order of reflection can be viewed separately as shown in Fig. 17. The superposition of the zero order and first order E-field makes the total E-field in Fig. 16(b). It is important to note that when the ray tubes hit the corners of the chamber, the wave front distorts drastically which may cause unreasonable values for the further rays, thus these ray tubes are filtered and may result in small errors.

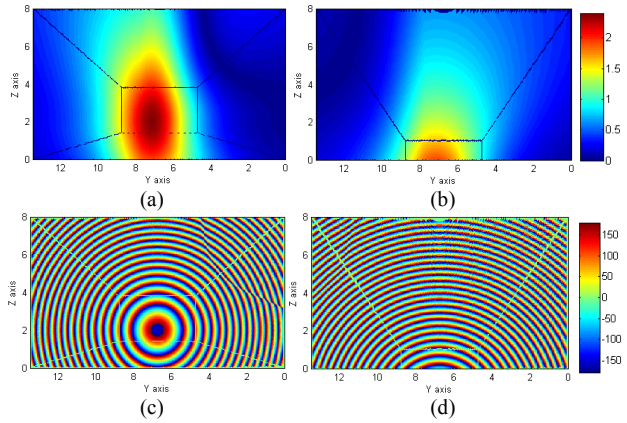

Fig. 17. *y*-polarized E-field with different reflective orders: (a) zero order magnitude, (b) first order magnitude, (c) zero order phase, (d) first order phase.

By using the inverse algorithm, the paths with less than the 2nd orders are shown in Fig. 18, higher order rays do not exist for the ideal semi-anechoic chamber. Actually only the zero and first order rays contribute to the field superposition, higher order rays are absorbed by the PML boundary.

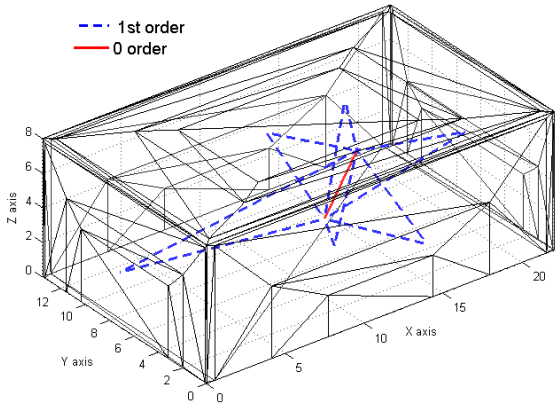

Fig. 18. Paths connect the source point and the field point with different orders: 1 ray with zero order and 6 rays with the first order.

The E-field values are extracted with the height scanning from 0 ~ 4 m at the center of the test region. Both the forward and inverse algorithms are used; results are compared and shown in Fig. 19. It can be seen that all the results are in good agreement except the height is close to the ceiling, this is because for the forward algorithm, the ray tubes hit the corners are filtered, the values become inaccurate when close to the corner (height close to 8 meters).

After the E-field values are extracted, (6) is used to obtain the NSA values. The same procedure is repeated for each frequency of interest, Fig. 20 gives the results obtained from the CISPR standard [7], the MoM method and FACET. It is important to note that when we use the half-wave dipole antenna, mutual coupling correction factors should be used. As can be seen in Fig. 20, all the curves agree well with each other. The difference (mainly at lower frequencies) between the MoM and the other two is mainly due to the non-typical balun of the Tx antenna as already stated in [7]. Also GO is a high frequency method: at lower frequencies, the accuracy of the proposed GO-based method is reduced.

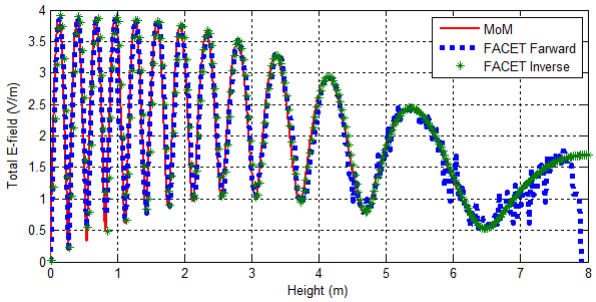

Fig. 19. Total E-field comparison by using different methods.

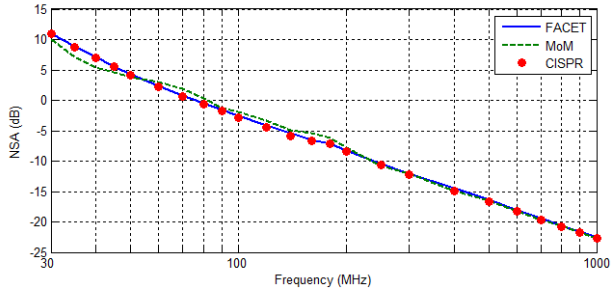

Fig. 20. NSA comparison of the reference semi-anechoic chamber.

For this scenario, the overall simulation time using FACET for each polarization is less than 1 minute with a standard PC. The results validate the proposed method with confidence. It should be noted that for a practical chamber it is not realistic to simulate it using MoM (a huge amount of memory requirement and complex material definition which is sometimes not known). Simulation and measurement results for a practical semi-anechoic chamber using FACET are compared in the next section.

V. Measurements And Comparisons

For measurement comparison, a semi-anechoic chamber is selected as shown in Fig. 21. The size is 22 m × 13.5 m × 8 m ($L \times W \times H$). Both 3 m and 10 m NSA values are measured following the standard steps in [7]. Four different locations of the Rx antenna in the turntable region are tested: left (L), right (R), front (F) and center (C). For each location, there are two height values and two polarizations for the Tx antenna. These make 2 × 2 × 4 = 16 cases for each distance as shown in Table III. A biconical antenna is used in the frequency range of 30 MHz ~ 200 MHz and a log-periodic antenna (LPDA) is used in

the frequency range of 200 MHz ~ 1 GHz. For the 10 m case, the Tx antenna is chosen to be 15° off the axis to test a more general scenario.

The layout of the RAM is given in Fig. 4, the color represents the RAM type. Each RAM was characterized and the complex reflection coefficients for different angles were obtained. The magnitude of the normal reflection coefficient is shown in Fig. 22. The paths with different orders for one of the receiving points are shown in Fig. 23. 100 sample points are used for the 1 m to 4 m height scanning. The rays up to the 2nd order are considered, and the convex acceleration is used. For each scenario, the resource consumption using the inverse algorithm is shown in Table IV. The resource consumption using the traditional FDTD has also been estimated and given in the table. It can be seen that the full wave method takes 8 hours and 10 GB memory to complete the simulation and is not a good choice for a chamber designer. For the frequency higher than 1 GHz or a larger chamber the problem will become even worse.

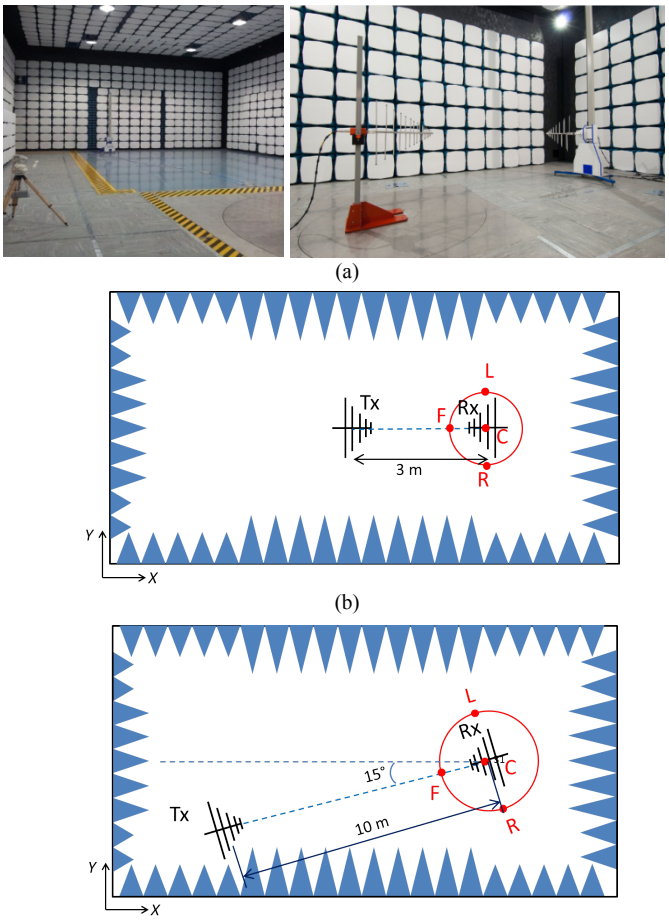

Fig. 21. NSA measurement scenario: (a) chamber under test, (b) 3 m NSA, (c) 10 m NSA.

The measurement results for the 3 m NSA values deviated from the CISRP standard [7] are shown in Fig. 24(a) ~ Fig. 24(d), the simulation results using FACET are shown in Fig. 24(e) ~ Fig. 24(h). The measured and simulated results agree well with each other, the spikes in the measurement results may be due to the unexpected scatters from the complex environment (cables, masts, imperfect ground); Fig. 25 gives the measured and simulated 10 m NSA deviation. It can be seen that they are correlated; the peak value may have a slight shift in frequency which is due to the phase error at lower frequencies (mutual coupling, near-field effect). The differences between the simulation and measurement values are within ±2 dB.

TABLE III
NSA TEST SCENARIOS

Polarization	Tx Height	Rx Location
Horizontal (H) Vertical (V)	Lower (L) Upper (U)	Left (L) Right (R) Front (F) Center (C)

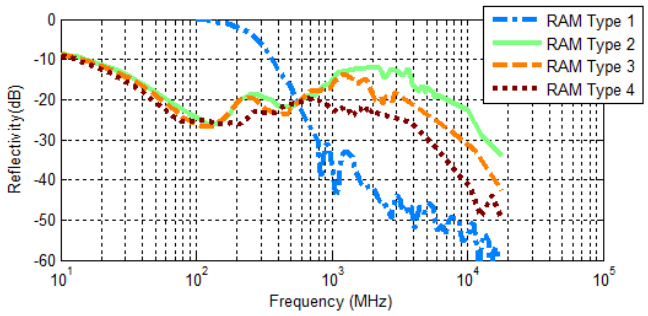

Fig. 22. Normal reflection coefficient for different types of RAM.

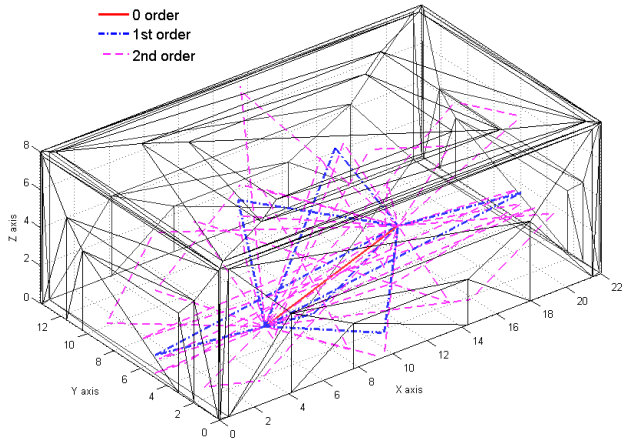

Fig. 23. Paths connect the source point and the field point with different orders: 1 ray with zero order, 6 rays with first order and 18 rays with second order.

TABLE IV
RESOURCE COMPARISON

	CPU	Mesh No.	Memory Requirement	Simulation Time
GO Inverse Algorithm	2.33GHz 2 threads	116 Triangles	~ 200 MB	2.5 mins
FDTD	3.0 GHz 4 threads	~ 90 million Hexahedra	~ 10 GB	~ 8 hrs

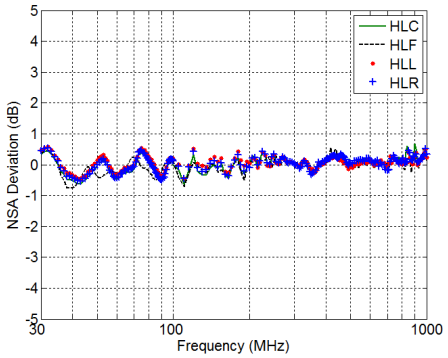

(a)

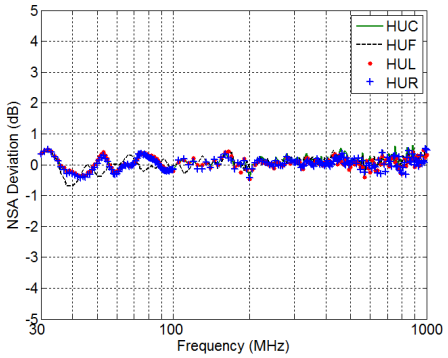

(b)

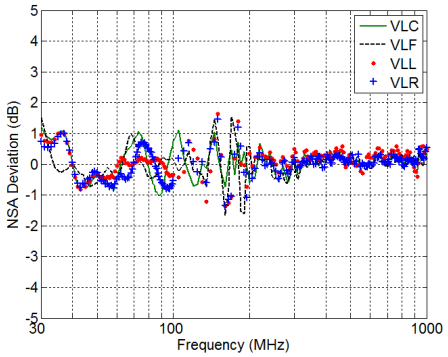

(c)

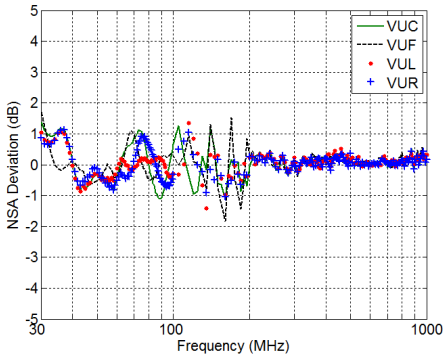

(d)

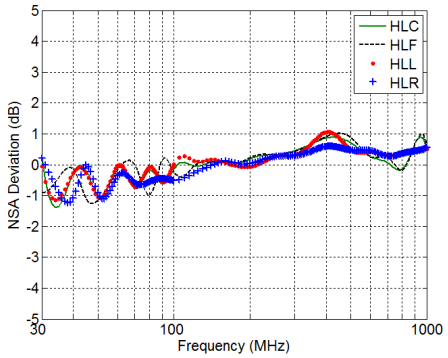

(e)

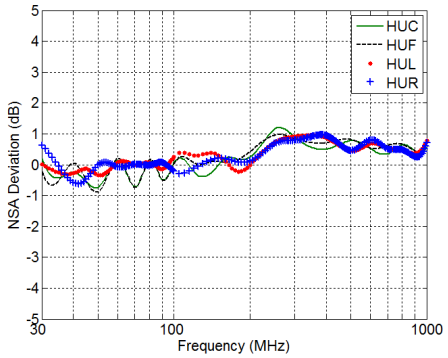

(f)

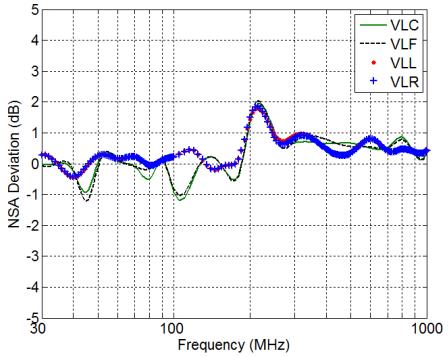

(g)

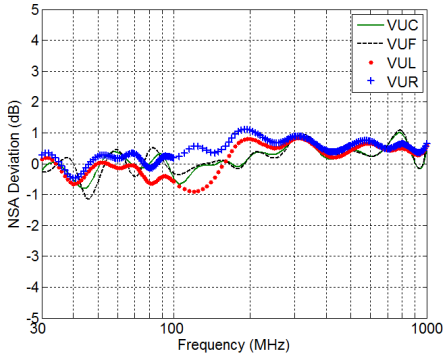

(h)

Fig. 24. 3 m NSA deviation values: (a) ~ (d) measurement results, (e) ~ (h) simulation results. The notations are explained in Table III, e.g. HLC stands for horizontal polarization (H), the Tx antenna at the lower (L) height and the Rx antenna is located at the center (C) of the test region.

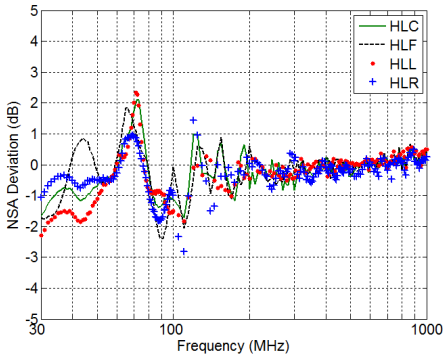

(a)

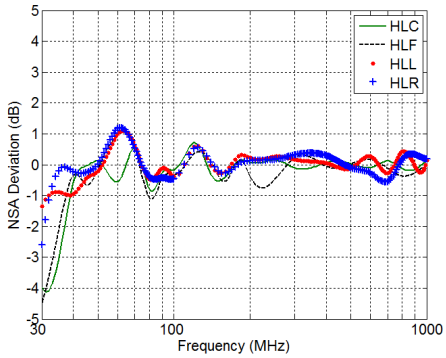

(e)

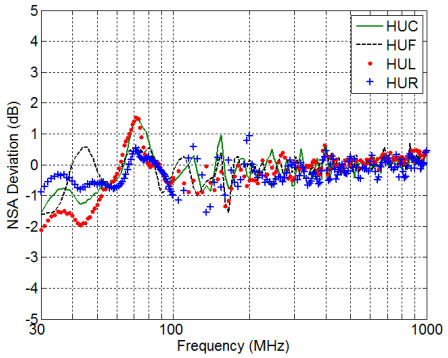

(b)

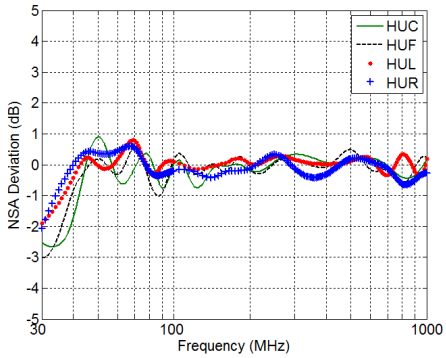

(f)

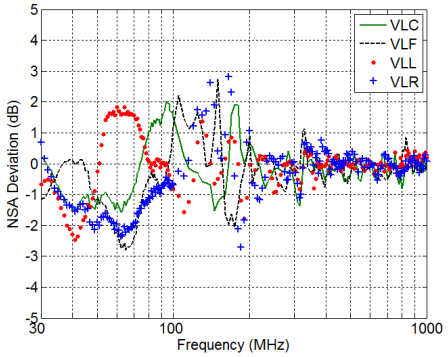

(c)

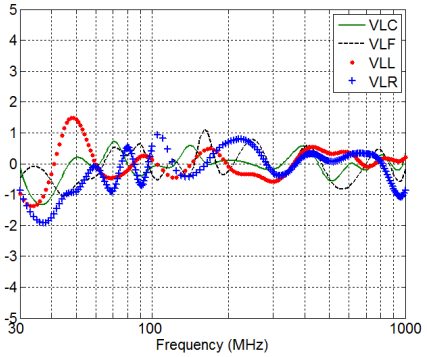

(g)

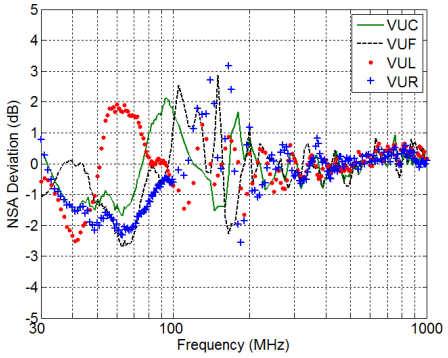

(d)

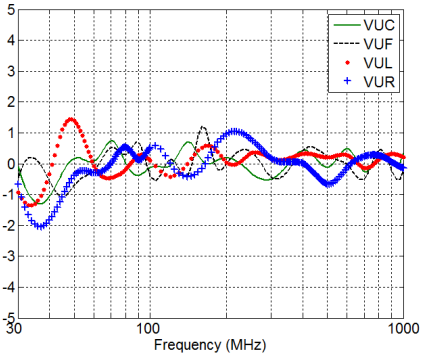

(h)

Fig. 25. 10 m NSA deviation values: (a) ~ (d) measurement results, (e) ~ (h) simulation results.

The simulation and measurement of the FU in the frequency range of 80 MHz to 6 GHz have also been conducted and good results were obtained [47]. The results show that: for the frequencies higher than 1 GHz, the difference is smaller than 2

dB for both polarizations. For the frequencies lower than 1 GHz, the error of FU in H-polarization is larger than that in V-polarization, this may be due to the mutual coupling between the Tx antenna and its image antenna, as the mutual coupling of the horizontal polarization is larger than vertical polarization.

VI. Discussion and Conclusions

A systematic solution has been proposed for anechoic chamber analysis and design which has resulted in the development of a CEM tool (FACET). The results from both the simulation and measurement have confirmed the validity and accuracy of the proposed solution. By borrowing the philosophy from software engineering, this approach does not require the antenna and RAM details which are normally not available. It provides a seamless connection between the micro level and the macro level designs, which makes the design procedure systematical. Although compared with the traditional analytical model, the proposed RAM model requires more memory to save it (10 MB/each type, it is still very small for computers nowadays) which is a trade-off of the proposed approach.

It has also been shown that the tool is efficient and accurate for the anechoic chamber simulation and suitable for real work chamber design. Two algorithms are developed: the forward algorithm is more efficient for P2A problems while the inverse algorithm is more suitable for P2P problems. The corresponding acceleration strategies have been proposed, developed and discussed in detail. The adaptive octree has been proposed for the forward algorithm, and a new acceleration strategy named convex acceleration has also been proposed for the inverse algorithm. Both have improved the efficiency significantly.

It is interesting to note the unique advantage of GO: fields with different orders can be viewed separately, this can be used to diagnose problems and identify where the unexpected field comes from.

It is important to note that the GO is a high frequency approximation method, in the measurement part we have compared the simulation and measurement results which were in good agreement, and the error was smaller than ± 2 dB. A potential problem is: at lower frequencies, the near field mutual coupling and diffraction may affect the results (the prediction accuracy is expected to be reduced using the proposed approach). However, in this case, the electrical size of the problem is not large; full-wave method can be used to simulate this problem [22-23]. Another issue is that the tip scattering of RAM at higher frequencies becomes significant and it is not considered in this model, when the tip scattering becomes the major contribution for the unexpected field (in millimeter wave), it will limit the boundary of the high frequency of this method. This could be in the region of statistical electromagnetics but not deterministic electromagnetics. For different RAM layout of the chamber the limit may vary, more detailed research for specific kinds of chambers will be the future work.

References

[1] W. H. Emerson, "Electromagnetic wave absorbers and anechoic chamber through the years," *IEEE Trans. Antennas Propagat.*, vol. 21, no. 4, pp. 484–490, Jul. 1973.

[2] L. H. Hemming, *Electromagnetic Anechoic Chambers: A Fundamental Design and Specification Guide*, New York: Wiley-IEEE Press, 2002.

[3] H. E. King, F. I. Shimabukuro and J. L. Wong, "Characteristics of a tapered anechoic chamber," *IEEE Trans. Antennas Propagat.*, vol. 15, no. 3, pp. 488–490, May 1967.

[4] V. Galindo-Israel, S. R. Rengarajan, W. A. Imbriale and R. Mittra, "Offset dual-shaped reflectors for dual chamber compact ranges," *IEEE Trans. Antennas Propagat.*, vol. 39, no. 7, pp. 1007–1013, Jul. 1991.

[5] L. H. Hemming, "Anechoic chamber," U.S. Patent 4 507 660, March 26, 1985.

[6] G. A. Sanchez, "Geometrically optimized anechoic chamber," U.S. Patent 5 631 661, May 20, 1997.

[7] *CISPR 16-1-4: Specification for radio disturbance and immunity measuring apparatus and methods - Part 1-4: Radio disturbance and immunity measuring apparatus - Antennas and test sites for radiated disturbance measurements*, IEC Standard, Ed 3.1, Jul. 2012.

[8] *IEC 61000-4-3: Electromagnetic compatibility (EMC) - Part 4-3: Testing and measurement techniques - Radiated, radio-frequency, electromagnetic field immunity test*, IEC Standard, Ed 3.1, Apr. 2008.

[9] K. Elmahgoub, F. Yang, A. Z. Elsherbeni, V. Demir and J. Chen, "FDTD analysis of periodic structures with arbitrary skewed grid," *IEEE Trans. Antennas Propagat.*, vol. 58, no. 8, pp. 2649–2657, Aug. 2010.

[10] W. Sun, K. Liu and C. A. Balanis, "Analysis of singly and doubly periodic absorbers by frequency-domain finite-difference method," *IEEE Trans. Antennas Propagat.*, vol. 44, no. 6, pp. 798–805, Jun. 1996.

[11] Y. Jiang and A. Q. Martin, "The design of microwave absorbers with high order hybrid finite element method," in *IEEE Antennas and Propagation Society International Symposium*, Orlando, 1999, vol. 4, pp. 2622–2625.

[12] R. Janaswamy, "Oblique scattering from lossy periodic surfaces with application to anechoic chamber absorbers," *IEEE Trans. Antennas Propagat.*, vol. 40, no. 2, pp. 162–169, Feb. 1992.

[13] N. Marly, B. Baekelandt, D. D. Zutter and H. F. Pues, "Integral equation modeling of the scattering and absorption of multilayered doubly-periodic lossy structures," *IEEE Trans. Antennas Propagat.*, vol. 43, no. 11, pp. 1281–1287, Nov. 1995.

[14] V. Kubytskyi, B. Sapoval, G. Dun and J. Rosnarho, "Fast optimization of microwave absorbers," *Microwave and Optical Technology Letters*, vol. 54, no. 11, pp. 2472-2477, Nov. 2012.

[15] E. F. Kuester and C. L. Holloway, "A low-frequency model for wedge or pyramid absorber arrays-I: theory," *IEEE Trans. Electromagnetic Compatibility*, vol. 36, no. 4, pp. 300-306, Nov. 1994.

[16] C. L. Holloway and E. F. Kuester, "A low-frequency model for wedge or pyramid absorber arrays-II: computed and measured results," *IEEE Trans. Electromagnetic Compatibility*, vol. 36, no. 4, pp. 307-313, Nov. 1994.

[17] A. Khajehpour and S. A. Mirtaheri, "Analysis of pyramid EM wave absorber by FDTD method and comparing with capacitance and homogenization methods," *Progress In Electromagnetics Research Letters*, vol. 3, pp. 123-131, 2008.

[18] M. G. Moharam, D. A. Pommet, E. B. Grann and T. K. Gaylord, "Stable implementation of the rigorous coupled-wave analysis for surface-relief gratings: enhanced transmittance matrix approach," *Journal of the Optical Society of America A*, vol. 12, iss. 6, pp. 1077-1086, 1995.

[19] T. Sasaki, Y. Watanabe and M. Tokuda, "NSA calculation of anechoic chamber using method of moment," in *Progress In Electromagnetics Research Symposium*, Cambridge, 2006, pp. 200-205.

[20] M. Kawabata, Y. Shimada, K. Shmada and N. Kuwabara, "FDTD method for site attenuation analysis of compact anechoic chamber using large-cell concept," *Electrical Engineering in Japan*, vol. 162, iss. 4, pp. 9-16. 2008.

[21] F. Bellamine, "Simulation of anechoic chamber using a combined TLM and homogenization method in the frequency range 30-200 MHz," in *First European Conference on Antennas and Propagation (EuCAP),* Nice, 2006, pp. 1-6.

[22] Available:https://www.cst.com/Applications/Article/Intelligent-Representation-Of-Anechoic-Chamber-Wall-Cuts-Electromagnetic-Simulation-Time-95.

[23] D. Campbell, G. Gampala, C. J. Reddy, M. Winebrand and J. Aubin, "Modeling and analysis of anechoic chamber using CEM tools," in *Proceedings of AMTA Conference*, Bellevue, 2012.

[24] N. V. Kantartzis and T. D. Tsiboukis, "Wideband numerical modelling and performance optimisation of arbitrarily-shaped anechoic chambers via an unconditionally stable time-domain technique," *Electrical Engineering*, vol. 88, iss. 1, pp. 55-81, Nov. 2005.

[25] B. K. Chung, C. H. The and H. T. Chuah, "Modeling of anechoic chamber using a beam-tracing technique," *Progress In Electromagnetics Research (PIER)*, vol. 49, pp. 23-38, 2004.

[26] S. R. Mishra and T. J. F. Pavlasek, "Design of absorber-lined chamber for EMC measurements using a geometrical optics approach," *IEEE Trans. Electromagnetic Compatibility*, vol. EMC-26, no. 3, pp. 111-119, Aug. 1984.

[27] M. K. Mansour and J. Jarem, "Anechoic chamber design using ray tracing and theory of images," in *IEEE Southeastcon '90 Proceedings*, New Orleans, 1990, pp. 689-695.

[28] C. L. Holloway and E. F. Kuester, "Modeling semi-anechoic electromagnetic measurement chambers," *IEEE Trans. Electromagnetic Compatibility*, vol. 38, no. 1, pp. 79-94, Feb. 1996.

[29] M. Lin, J. Ji, C. G. Hsu and H. Hsieh, "Simulation and analysis of EMC chambers by ray tracing method," in *IEEE International Symposium on Electromagnetic Compatibility*, Honolulu, 2007, pp. 1-4.

[30] S. M. J. Razavi, M. Khalaj-Amirhosseini and A. Cheldavi, "Minimum usage of ferrite tiles in anechoic chambers," *Progress In Electromagnetics Research B (PIER B)*, vol. 19, pp. 367-383, 2010.

[31] B. K. Chung, H. T. Chuah, "Modeling of RF absorber for application in the design of anechoic chamber," *Progress In Electromagnetics Research, (PIER)*, vol. 43, pp. 273-285, 2003.

[32] M. F. Catedra. J. Perez, F. Saez de Adana and O. Gutierrez, "Efficient ray-tracing techniques for three-dimensional analyses of propagation in mobile communications: application to picocell and microcell scenarios," *IEEE Antennas and Propagation Magazine*, vol. 40, no. 2, pp. 15-28, Apr. 1998.

[33] C. A. Balanis, *Advanced Engineering Electromagnetics*, John Wiley & Sons, 1989.

[34] C. Yang, B. Wu and C. Ko "A ray-tracing method for modeling indoor wave propagation and penetration," *IEEE Trans. Antennas Propagat.*, vol. 46, no. 6, pp. 907–919, Jun. 1998.

[35] A. S. Glassner, *An Introduction to Ray Tracing*, Morgan Kaufmann, 1989.

[36] C. Saeidi, A. Fard and F. Hodjatkashani, "Full three-dimensional radio wave propagation prediction model," *IEEE Trans. Antennas Propagat.*, vol. 60, no. 5, pp. 2462–2471, May 2012.

[37] K. Jin, T. Suh, S. Suk, B. Kim and H. Kim "Fast ray tracing using a space-division algorithm for RCS prediction," *Journal of Electromagnetic Waves and Applications*, vol. 20, no. 1, pp. 119-126, 2006.

[38] Y. Tao, H. Lin and H. Bao, "Kd-tree based fast ray tracing for RCS prediction," *Progress In Electromagnetics Research, (PIER)*, vol. 81, pp. 329-341, 2008.

[39] M. Ohta and M. Maekawa, "Ray coherence theorem and constant time ray tracing algorithm," *Computer Graphics*, pp. 303-314, 1987.

[40] J. Bang and B. Kim "Time consumption reduction of ray tracing for RCS prediction using efficient grid division and space division algorithms," *Journal of Electromagnetic Waves and Applications*, vol. 21, no. 6, pp. 829-840, 2007.

[41] H. Meng, "Acceleration of asymptotic computational electromagnetics physical optics – shooting and bouncing ray (PO-SBR) method using CUDA," M.S. thesis, Dept. Electrical and Computer Eng., University of Illinois at Urbana-Champaign., Illinois, USA, 2011.

[42] J. W. McKown and R. L. Hamilton , "Ray tracing as a design tool for radio networks," *IEEE Network*, vol. 5, no. 6, pp. 27-30, Nov. 1991.

[43] M. Bruns, *Automated Fabrication: Improving Productivity in Manufacturing*, Prentice Hall, 1993.

[44] *IEEE Std 1128-1998: IEEE Recommended Practice for Radio-Frequency (RF) Absorber Evaluation in the Range of 30 MHz to 5 GHz*, IEEE Standard, Apr. 1998.

[45] V. P. Kodali, *Engineering Electromagnetic Compatibility: Principles, Measurements, Technologies, and Computer Models*, 2nd Ed, New York: Wiley-IEEE Press, 2001

[46] T. H. Cormen, C. E. Leiserson, R. L. Rivest and C. Stein, *Introduction to Algorithms,* 3rd Ed, The MIT Press, 2009.

[47] Q. Xu, Y. Huang, X. Zhu, L. Xing, P. Duxbury and J. Noonan, "An efficient method for the field uniformity analysis of anechoic chambers," in *IEEE International Symposium on Antennas and Propagation*, Memphis, 2014.